Atomic-Scale Elucidation of Formation and Structure in High-Performance Re-Ge Nanocatalysts

Masahiko Shimizu,*[a,b,c] Yuta Inami,[a] Ryuichi Shimogawa,[a,d] Takeshi Matsuo,[a] Yu Fujikata,[a] Hajime Matsumoto,[a,b] Kazutaka Mitsuishi*[e] and Ayako Hashimoto*[b,c]

a. Science & Innovation Center, Mitsubishi Chemical Corporation, 1000 Kamoshida-cho, Aoba-ku, Yokohama, Kanagawa, Japan.
b. Research Center for Energy and Environmental Materials, National Institute for Materials Science, 1-2-1 Sengen, Tsukuba, Ibaraki, Japan.
c. Graduate School of Science and Technology, University of Tsukuba, 1-2-1 Sengen, Tsukuba, Ibaraki, Japan.
d. Department of Materials Science and Chemical Engineering, Stony Brook University, Stony Brook, New York 11794, United States
e. Center for Basic Research on Materials, National Institute for Materials Science, 1-2-1 Sengen, Tsukuba, Ibaraki, Japan.

Table of Contents

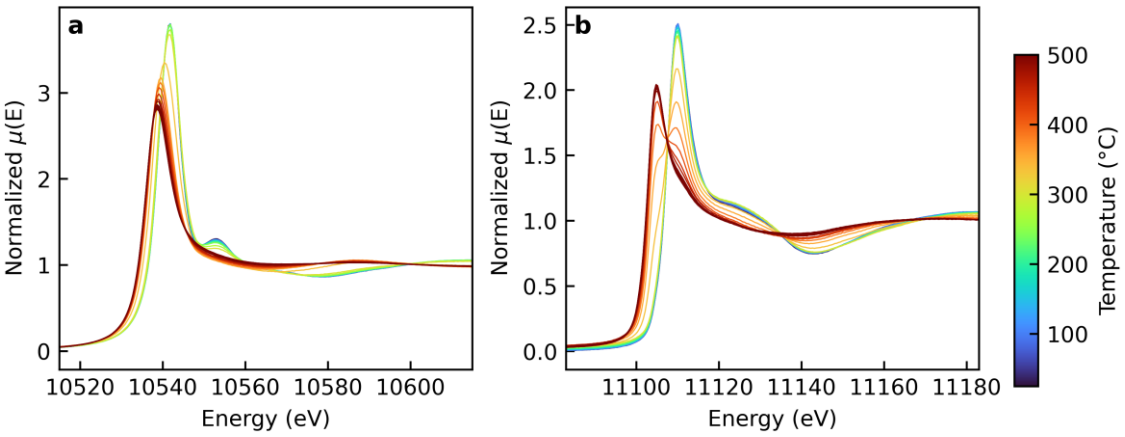

Figure S1 X-ray absorption near edge structure (XANES) spectra of Re-Ge/TiO_2 during hydrogen reduction as a function of temperature. (a) Re L_3 edge XANES spectra showing the evolution from oxidized to reduced Re species. (b) Ge K edge XANES spectra during reduction. The color scale ranges from room temperature (blue) to 500 °C (red).

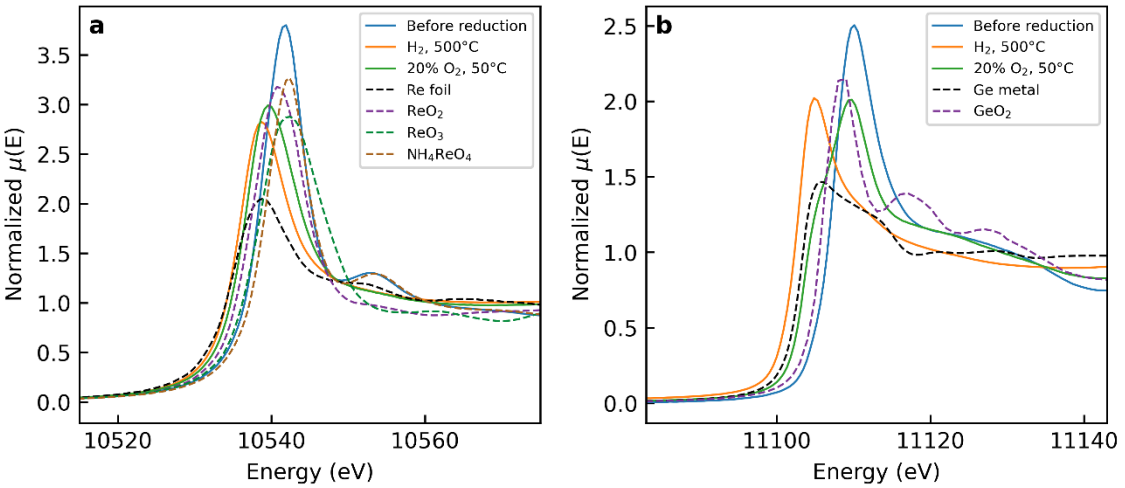

Figure S2 X-ray absorption near edge structure (XANES) spectra of Re-Ge/TiO_2 at different stages of the preparation compared with reference compounds. (a) Re L_3 edge XANES spectra with reference compounds: Re foil (black dashed), ReO_2 (purple dashed), ReO_3 (green dashed), NH_4ReO_4 (brown dashed). (b) Ge K edge XANES spectra with reference compounds: Ge metal (black dashed), hexagonal GeO_2 (purple dashed). Sample spectra are shown before hydrogen reduction (blue), after hydrogen reduction at 500 °C (orange), and after exposure to 20 % O_2 at 50 °C (green).

Details of the EXAFS Fitting

EXAFS fitting was performed with the Larch software package[1] with FEFF8.5L for scattering path calculations. Fitting was performed in R-space, and the variable parameters included coordination numbers N, bond distance changes ΔR, Debye-Waller factors σ^2, and energy shifts ΔE_0, which are shown below.

For Re L_3 edge fitting, the amplitude reduction factor (S_0^2 = 0.78) was determined by fitting the NH_4ReO_4 reference compound with the known tetrahedral ReO_4 coordination (N = 4) and was fixed in subsequent analyses. For scattering path calculations, the NPr_4ReO_4 (tetrapropylammonium perrhenate) structure[2] was used, which is a well-defined tetrahedral structure. For samples at temperatures below 320 °C, the Re-O scattering path was calculated from the NPr_4ReO_4 structure. For samples at temperatures above 320 °C, the R-O path from the ReO_2 structure,[3] and the Re-Ge path from the Re_4Ge_7 intermetallic structure[4] were used for the fitting.

Fitting was performed over the R-range of 1.1–3.0 Å with k^3-weighted EXAFS data (k-range: 2.5–10 $Å^{-1}$). For two-shell fits, ΔE_0 was shared between paths. At the transition temperature (approximately 335 °C), where both short and long Re-O coordination coexist, a three-shell model was used that combined Re-O paths from both NPr_4ReO_4 (short) and ReO_2 (long) with the Re-Ge path, with σ^2(Re-O) shared between the two Re-O paths.

For the Ge K edge fitting, the amplitude reduction factor (S_0^2 = 1.00) was determined from fitting the hexagonal GeO_2 reference compound[5] with the known coordination (N = 4). The Ge-O scattering path was calculated from the hexagonal GeO_2. Fitting was performed using k^2-weighted EXAFS data (k-range: 2–10 $Å^{-1}$). Single-shell Ge-O fitting (R-range: 1.0–2.0 Å) was applied for samples before reduction, after cooling under hydrogen (50 °C), and after O_2 exposure (50 °C). For the sample reduced at 500 °C under hydrogen, a two-shell model (Ge-O + Ge-Re) with extended R-range (1.0–3.0 Å) was used, where the Ge-Re path was calculated from the Re_4Ge_7 structure, with ΔE_0 shared between paths. To evaluate whether the second coordination shell around Ge at 500 °C corresponds to Re or Ge neighbors, an alternative two-shell model (Ge-O + Ge-Ge) was fitted. The Ge-Ge path was calculated from the Ge metal structure.[6] The model comparison is presented in Table S1.

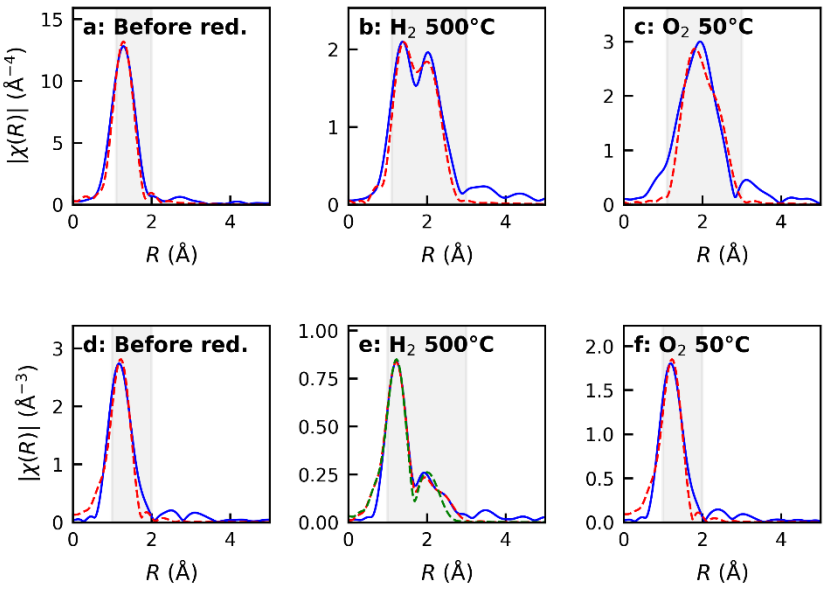

Figure S3 Extended X-ray absorption fine structure fitting results in R-space for Re-Ge/TiO_2 samples. Top row (a-c): Re L_3 edge fits (k-range: 2.5-10 $Å^{-1}$, k-weight: 3, R-range: 1.1-3.0 Å). (a) Uses a single-shell Re-O fit; panels (b, c) use two-shell Re-O + Re-Ge fits. Bottom row (d-f): Ge K edge fits (k-range: 2-10 $Å^{-1}$, k-weight: 2). (e) Uses two-shell Ge-O + Ge-Re fit (R-range: 1.0-3.0 Å); (d, f) use single-shell Ge-O fits (R-range: 1.0-2.0 Å). Blue solid: data, Red dashed: fit, Green dashed: alternative Ge-Ge fit (panel e only), Gray shaded: fitting window.

Table S1 Alternative two-shell extended X-ray absorption fine structure fitting for Re-Ge/TiO_2 at 500°C (Ge-O + Ge-Ge)

Path	N	R (Å)	σ^2 (×10^{-3} Å²)	ΔE_0 (eV)	R-factor	χ_ν^2
Ge-O	1.5±0.5	1.758±0.022	0.0±0.7	-4.1±4.1	3.3 %	55.0
Ge-Ge	1.2±1.3	2.431±0.033	10.9±0.0			

Table S2 Re L_3 edge temperature-dependent two-shell fitting results. Labels (a–s) correspond to spectra continuously collected during hydrogen reduction, as shown in Figure S5.

Label	T (°C)	Re-O path	*N*(Re-O)	*R*(Re-O) (Å)	*N*(Re-Ge)	*R*(Re-Ge) (Å)	*R*-factor(%)
a	25	NPr_4ReO_4	5.3±2.0	1.708±0.024	0.3±1.9	2.496±0.108	2.8
b	55	NPr_4ReO_4	5.3±2.0	1.707±0.024	0.3±1.9	2.496±0.107	2.9
c	85	NPr_4ReO_4	5.3±2.0	1.708±0.024	0.3±1.9	2.498±0.104	2.9
d	105	NPr_4ReO_4	5.3±2.0	1.708±0.024	0.3±1.9	2.500±0.086	2.8
e	135	NPr_4ReO_4	5.3±2.1	1.703±0.025	0.3±1.9	2.491±0.084	2.9
f	165	NPr_4ReO_4	5.4±2.1	1.702±0.025	0.5±1.9	2.484±0.067	2.9
g	195	NPr_4ReO_4	5.4±2.2	1.696±0.026	0.5±2.0	2.484±0.067	3.0
h	215	NPr_4ReO_4	5.4±2.2	1.696±0.026	0.5±2.0	2.482±0.061	3.0
i	245	NPr_4ReO_4	5.1±1.9	1.697±0.027	0.5±1.9	2.485±0.062	3.3
j[1]	275	NPr_4ReO_4	4.7	1.697	0.7	2.487	3.6
k	305	NPr_4ReO_4	4.3±2.0	1.676±0.027	0.6±1.5	2.464±0.050	3.0
l[2]	335	3-shell**	3.9±3.4	1.66±0.06 1.93±0.11	0.7±1.3	2.457±0.103	1.7
m	355	ReO_2	3.0±1.9	1.936±0.065	0.7±1.9	2.445±0.069	7.4
n	385	ReO_2	2.6±1.9	1.940±0.069	0.9±1.7	2.453±0.064	7.1
o	415	ReO_2	2.4±1.9	1.931±0.074	0.9±1.6	2.450±0.065	7.2
p	445	ReO_2	2.6±2.1	1.924±0.079	0.8±1.8	2.437±0.076	8.1
q	465	ReO_2	2.1±1.8	1.924±0.077	0.8±1.5	2.443±0.069	7.4
r	495	ReO_2	2.2±2.1	1.912±0.081	0.8±1.6	2.436±0.072	7.9
s[3]	500	ReO_2	1.2±1.4	1.899±0.074	2.8±3.3	2.448±0.066	4.9

[1]Error estimation was not available because the parameters converged at constraint boundaries, precluding reliable uncertainty estimation. [2]The fit at 335 °C were performed with Re-O(short), Re-O(long), and Re-Ge paths. [3]Entry (s) values are from merged 500 °C spectra (8 scans) fitted with the same two-shell model as Table 2.

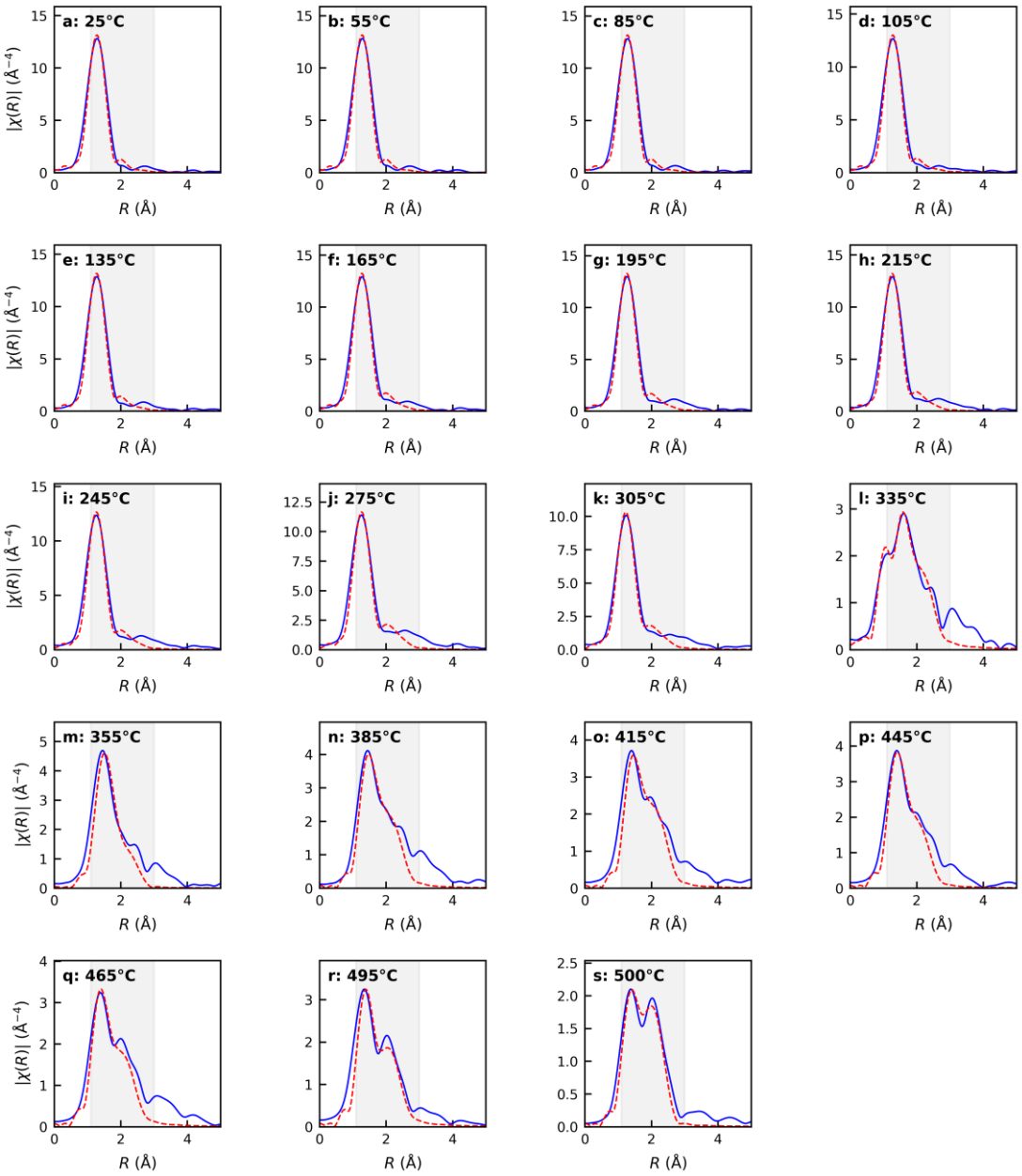

Figure S4 Temperature-dependent Re L_3 edge extended X-ray absorption fine structure fits in R-space for Re-Ge/TiO_2 during hydrogen reduction (k-range: 2.5-10 $Å^{-1}$, k-weight: 3, R-range: 1.1-3.0 Å). Each panel shows the fit at the indicated temperature. Blue solid: data, Red dashed: fit, Gray shaded: fitting window. (s) The fit at 500 °C is based on merged spectra (8 scans) to improve the signal-to-noise ratio.

Table S3 Ge K edge temperature-dependent single-shell fitting results. Labels (a–s) correspond to spectra continuously collected during hydrogen reduction, as shown in Figure S6.

Label	T (°C)	N(Ge-O)	R(Ge-O) (Å)	σ^2(Ge-O) ($\times 10^{-3}$ Å^2)	R-factor(%)
a	25	4.7±2.2	1.729±0.034	0.0±5.1	5.0
b	55	4.7±2.3	1.730±0.035	0.3±5.3	5.3
c	85	4.6±2.2	1.728±0.034	0.0±82.4	5.0
d	105	4.6±2.1	1.727±0.033	0.0±0.3	4.9
e	135	4.6±2.1	1.726±0.033	0.0±0.2	4.7
f	165	4.6±2.1	1.724±0.032	0.0±0.1	4.5
g	195	4.6±2.1	1.723±0.032	0.0±5351.9	4.5
h	215	4.6±2.0	1.724±0.031	0.0±7.2	4.3
i	245	4.6±2.1	1.721±0.031	0.0±5.1	4.3
j	275	4.6±2.1	1.721±0.032	0.0±6.1	4.4
k	305	4.6±2.0	1.722±0.031	0.0±3.0	4.2
l	335	3.8±1.5	1.727±0.029	0.0±5.0	3.7
m	355	3.0±1.2	1.734±0.028	0.0±1.1	3.4
n	385	2.5±1.1	1.744±0.031	0.3±4.8	4.3
o	415	2.2±1.0	1.760±0.032	0.1±4.8	4.7
p	445	2.1±1.2	1.765±0.041	1.6±6.3	6.9
q	465	1.9±1.1	1.767±0.042	0.9±6.4	7.4
r	495	1.8±1.0	1.772±0.042	1.7±6.5	7.2
s[1]	500	1.7±1.1	1.761±0.046	1.0±7.0	8.5

All entries use a single-shell (Ge-O only) fitting. [1]Entry (s) is from merged 500°C spectra (8 scans).

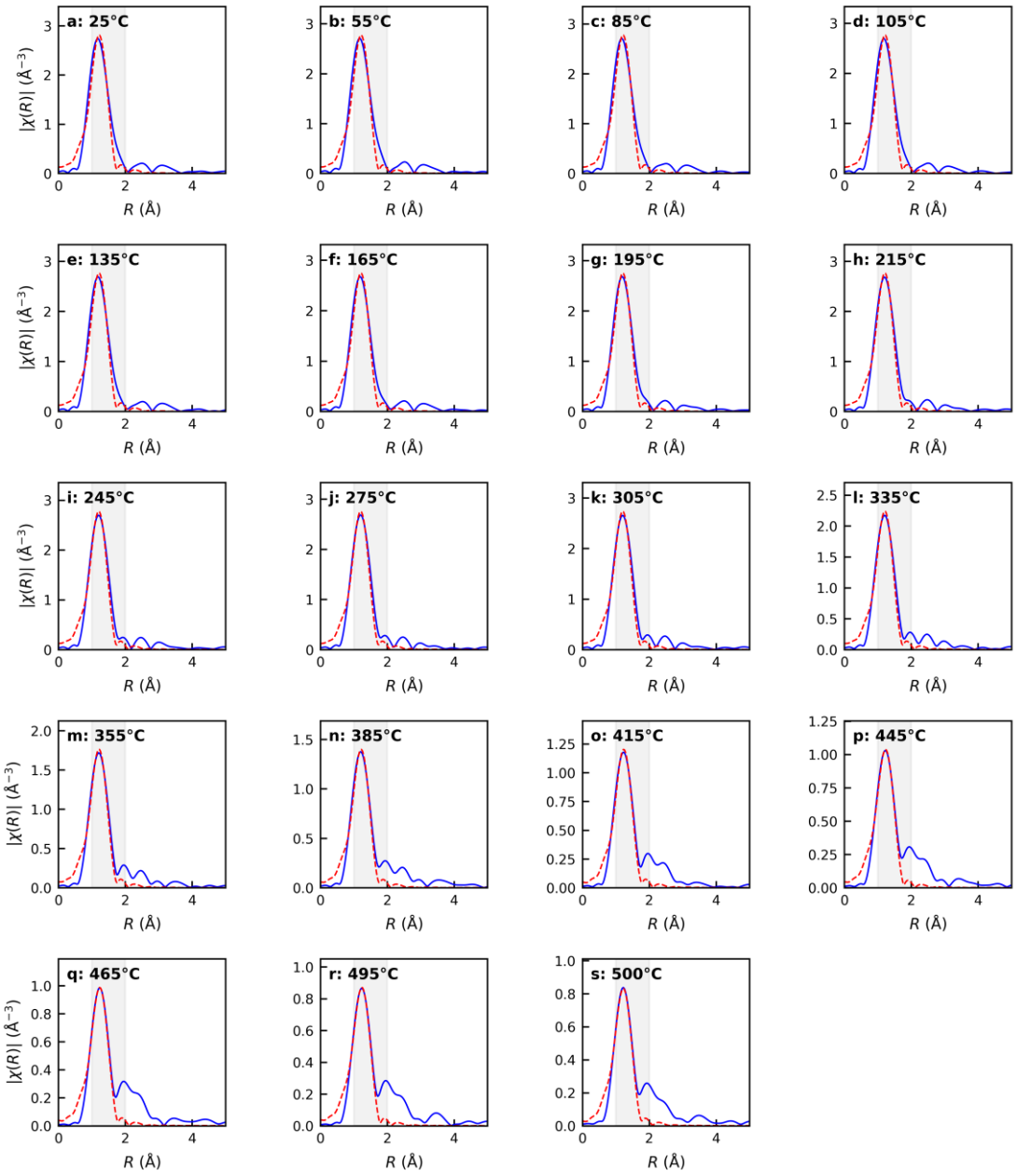

Figure S5 Temperature-dependent Ge K edge extended X-ray absorption fine structure fits in R-space for Re-Ge/TiO_2 during hydrogen reduction (k-range: 2-10 $Å^{-1}$, k-weight: 2, R-range: 1.0-2.0 Å). Each panel shows the fit at the indicated temperature. Blue solid: data, Red dashed: fit, Gray shaded: fitting window. Panel (s) at 500 °C is from merged spectra (8 scans) for improved signal-to-noise ratio.

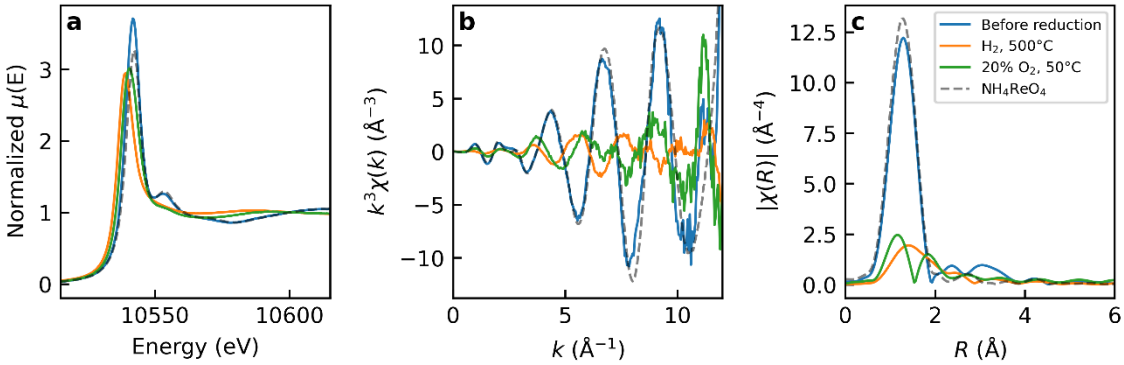

Figure S6 X-ray absorption fine structure (XAFS) analysis of Re/TiO_2 catalyst. (a) X-ray absorption near edge structure spectra, (b) k^3-weighted extended XAFS oscillations, and (c) Fourier transform magnitude. Data are shown for: before hydrogen reduction (blue), hydrogen reduction at 500 °C (orange), and after exposure to 20 % O_2 at 50 °C (green). NH_4ReO_4 reference is shown as a dashed line.

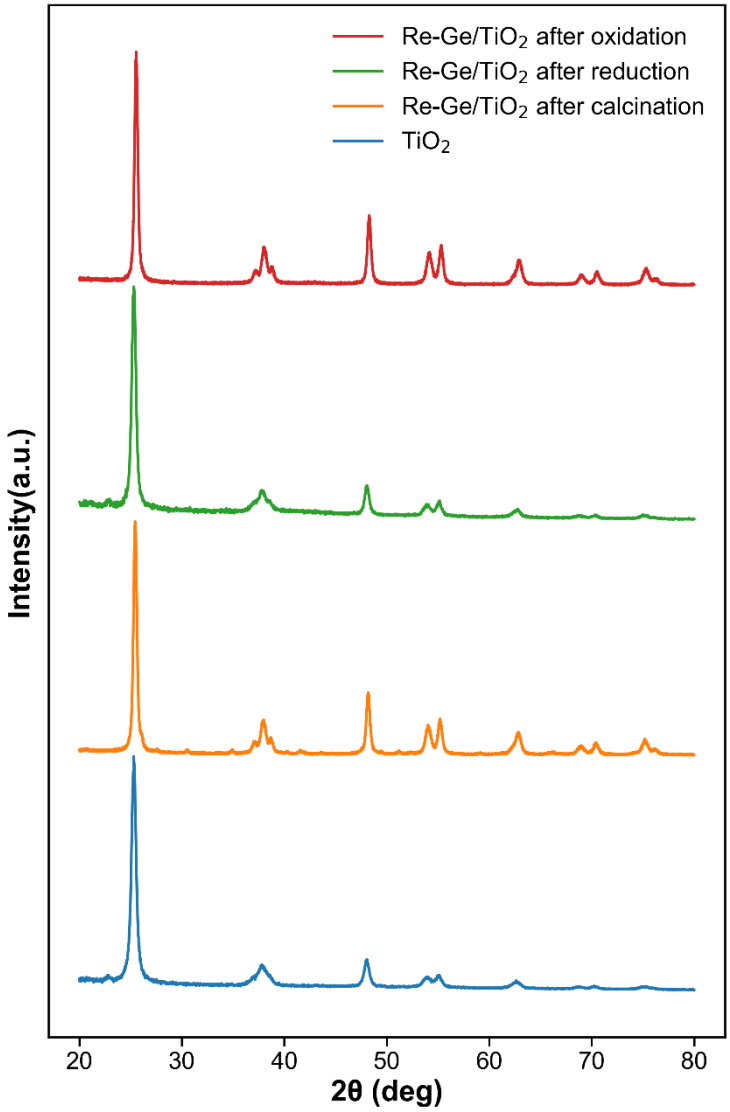

Figure S7 X-ray diffraction (XRD) patterns of the Re-Ge/TiO_2 catalyst at different treatment stages. From bottom to top: bare TiO_2 support (blue), Re-Ge/TiO_2 after calcination (orange), Re-Ge/TiO_2 after hydrogen reduction at 500 °C (green), Re-Ge/TiO_2 after oxidative stabilization (red). All the patterns are normalized to the maximum intensity and vertically offset to prevent overlapping. In all cases, only TiO_2-derived diffraction peaks were observed. Although slight differences in peak appearance are observed between the first (bare TiO_2 support) and third (after hydrogen reduction) patterns and the second (after calcination) and fourth (after oxidative stabilization) patterns, these differences are attributed to the use of different XRD instruments and measurement conditions.

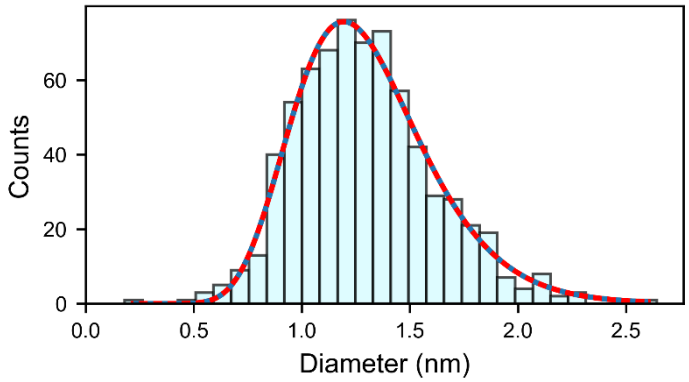

Figure S8 Particle size distribution of nanoparticles after hydrogen reduction. The diameters of 696 particles were measured according to a reported method.[7] Fitting the distribution with a log-normal function[8] yielded an average diameter of 1.3 ± 0.3 nm.

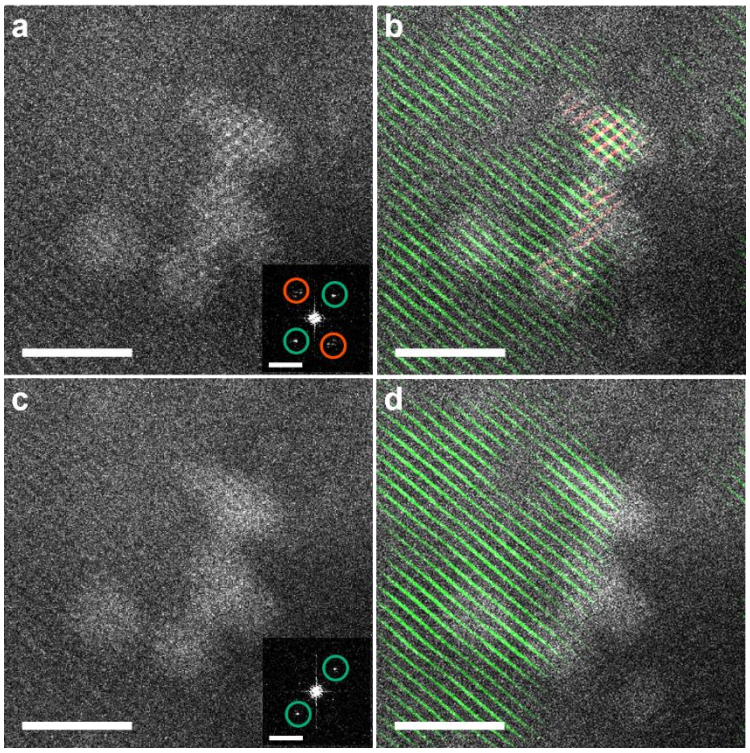

Figure S9 (a) High-angle annular dark-field scanning transmission electron microscopy (HAADF-STEM) image of a nanoparticle after hydrogen reduction. The inset shows the corresponding fast Fourier transform (FFT) pattern. (b)Composite image showing the HAADF-STEM image from (a) superimposed with images reconstructed from specific regions of its FFT pattern. The red-colored lattice fringes were obtained by inverse FFT from the spots enclosed by the red circles, while the green-colored fringes were from the spots enclosed by the green circles. (c) HAADF-STEM image of the same nanoparticle after oxidative stabilization. The inset shows the corresponding FFT pattern. (d) A composite image of the nanoparticle in (c), created using the same procedure as in (b). Scale bars: 2 nm (real space), 5 nm^{-1} (FFT).

Note:

The spots indicated by the green circles correspond to the crystal lattice of the TiO_2 support, while the spots indicated by the red circles correspond to the crystal lattice of the nanoparticles. The observation of lattice fringes originating from the TiO_2 support in both images (after hydrogen reduction and after oxidative stabilization) indicates that no significant defocus or residual aberrations were present during the measurements. Lattice fringes are visible within the nanoparticle after hydrogen reduction, whereas these nanoparticle-derived fringes disappear completely after oxidative stabilization. Therefore, the oxidative stabilization process is considered to decrease the nanoparticle crystallinity.

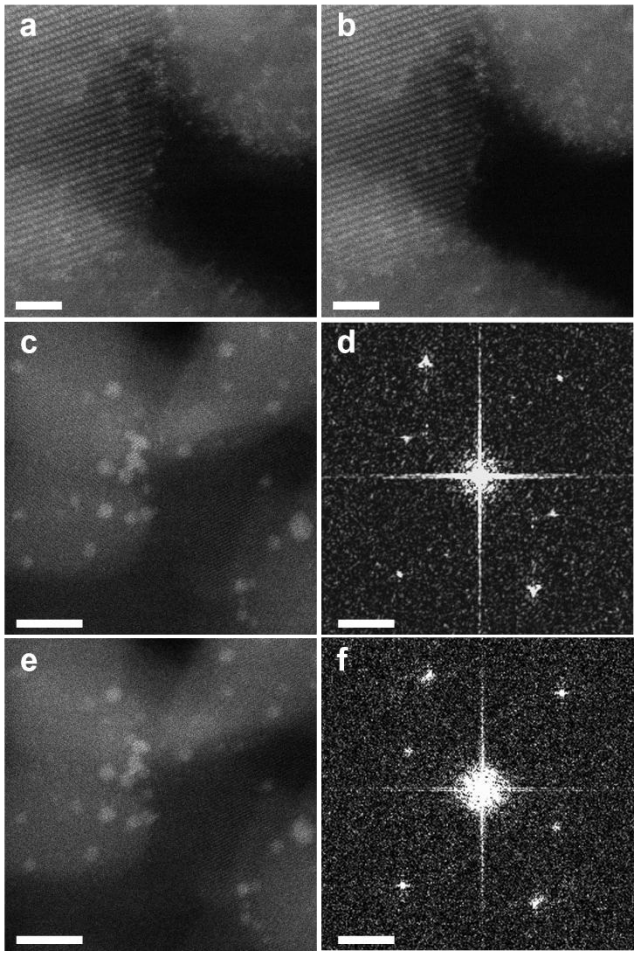

Figure S10 Electron-beam irradiation control experiments. (a,b) High-angle annular dark-field scanning transmission electron microscopy (HAADF-STEM) images of the same region of the calcined sample before (a) and after (b) irradiation of a 19.5 nm × 19.5 nm area for 35 s (dose: 1.2×10^5 e/Å^2, dose rate: 3.3×10^3 e/(Å^2·s)); no morphological change was observed and no crystalline ~1 nm nanoparticles, as observed after hydrogen reduction, appeared. (c,e) HAADF-STEM images of the reduced sample before (c) and after (e) irradiation of a 38.9 nm × 38.9 nm area for 20 s (dose: 1.7×10^4 e/Å^2, dose rate: 8.3×10^2 e/(Å^2·s)), showing no apparent structural change. (d,f) Corresponding fast Fourier transform (FFT) patterns of the HAADF-STEM images in (c) and (e), respectively, demonstrating that the FFT spot pattern is maintained and that the amorphization observed after oxidative stabilization (loss of FFT spots) is not induced by electron-beam exposure. Scale bars: 2 nm in (a-b); 5 nm in (c, e); 5 nm^{-1} in (d, f).

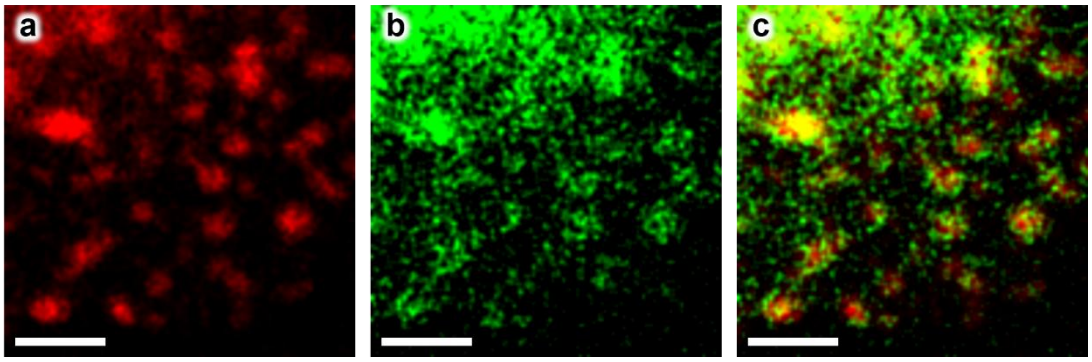

Figure S11 Scanning transmission electron microscopy-energy dispersive X-ray spectroscopy (STEM-EDS) elemental maps of the Re-Ge/TiO_2 catalyst after HYDROGEN reduction. (a) Re M map. (b) Ge L map. (c) Superimposed map of (a) and (b), corresponding to Figure 5a in the main text. Scale bar: 5 nm.

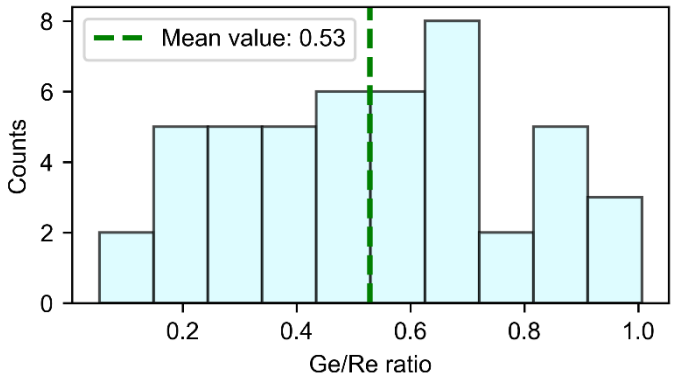

Figure S12 Histogram of the Ge/Re atomic ratio for individual nanoparticles after hydrogen reduction, as determined by scanning transmission electron microscopy-energy dispersive X-ray spectroscopy. Both Re and Ge were detected in all 48 particles analyzed. No particles with a Ge/Re ratio greater than one were found. The average Ge/Re atomic ratio was determined to be 0.53 ± 0.25.

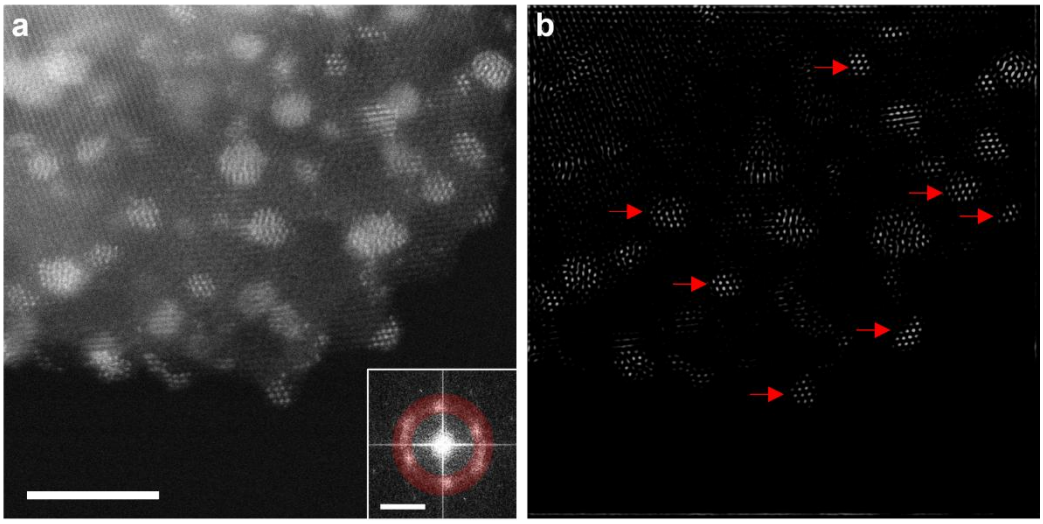

Figure S13 (a) High-angle annular dark-field scanning transmission electron microscopy image of the Re-Ge/TiO_2 catalyst after hydrogen reduction. The inset shows the corresponding fast Fourier transform (FFT) pattern of the area shown in (a). (b) The inverse FFT image reconstructed from the region enclosed by the red annulus in the inset of (a). The red arrows indicate a representative nanoparticle where a clear hexagonal atomic structure is visible.

Table S4 Best-matching view direction for distorted hexagonal close-packed (HCP) Re. The table summarizes, for each combination of a-axis strain ε_a and c-axis strain ε_c (in %), the zone-axis index that provides the closest match to the experimentally obtained fast Fourier transform (FFT) pattern. The reference lattice parameters of HCP Re were a=2.781 Å and c=4.497 Å[9]. In each cell, the upper entry indicates the zone-axis index of the closest view direction identified by SingleCrystal[10] (CrystalMaker Software Ltd.), and the value in parentheses gives the corresponding sum-of-squares error (SSE) between the experimental FFT pattern and the simulated diffraction pattern. The resulting zone-axis indices were limited to two types, [111] and [$\bar{1}$11]. For comparison, the SSE value obtained for the density functional theory derived face-centered cubic fragment (FCCf) structure (Figure S15) was 0.0088, which is substantially smaller than all SSE value listed in this table. The corresponding real-space atomic models and simulated diffraction patterns for the distorted HCP Re models viewed along the [111] and [$\bar{1}$11] zone axes, together with the FCCf structure are shown in Figure S14.

ε_c(%) / ε_a(%)	**-9**	**-6**	**-3**	**0**	**+3**	**+6**	**+9**
-9	111 (0.1541)	-	-	111 (0.1143)	-	-	111 (0.1374)
-6	-	111 (0.0994)	-	111 (0.0692)	-	111 (0.1343)	-
-3	-	-	111 (0.1136)	111 (0.1008)	111 (0.1133)	-	-
0	111 (0.1727)	111 (0.0975)	111 (0.1151)	111 (0.2206)	111 (0.1283)	111 (0.1096)	$\bar{1}$11 (0.1169)
+3	-	-	111 (0.1885)	111 (0.1639)	111 (0.1632)	-	-
+6	-	111 (0.1885)	-	$\bar{1}$11 (0.1571)	-	$\bar{1}$11 (0.1169)	-
+9	$\bar{1}$11 (0.3320)	-	-	$\bar{1}$11 (0.0986)	-	-	$\bar{1}$11 (0.0329)

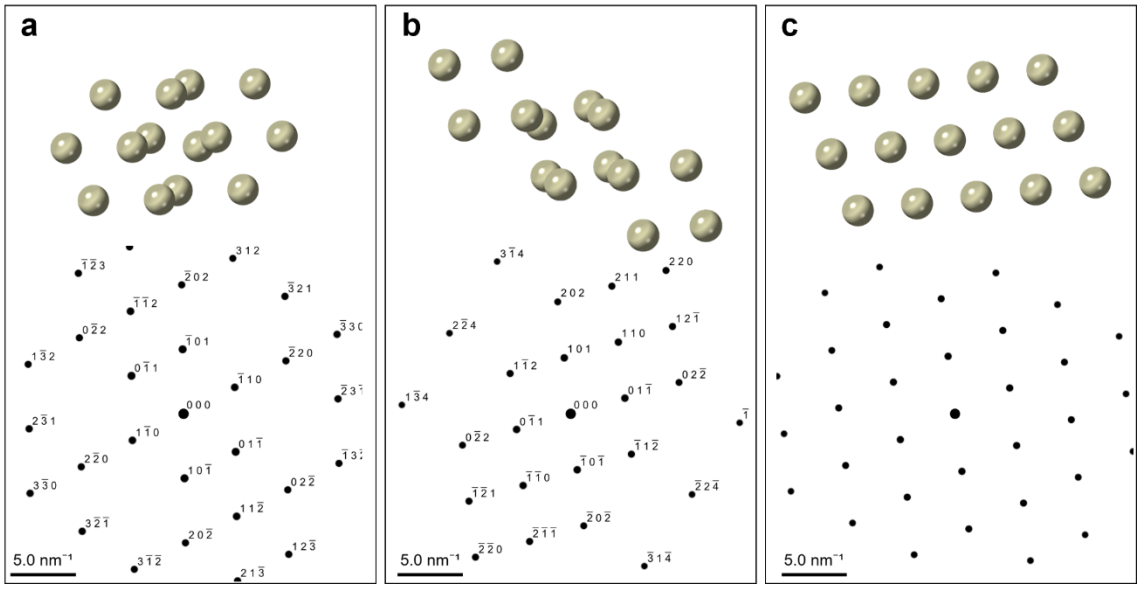

Figure S14 Real-space atomic arrangements and the corresponding simulated diffraction patterns for the hexagonal close-packed (HCP) Re structure and the density functional theory derived the face-centered cubic fragment (FCCf) structure (Figure S15). Real-space atomic models (top) and the corresponding simulated diffraction patterns (bottom) are shown for (a) the [111] zone axis, (b) the [$\bar{1}$11] zone axis, and (c) the FCCf structure. The [111] and [$\bar{1}$11] cases represent distorted HCP Re structures with the smallest SSE for each zone axis (as listed in Table S4): the [111] case corresponds to ε_a = -6 % and ε_c = -6 %, and the [$\bar{1}$11] case corresponds to ε_a = +9 % and ε_c = +9 %. Among the compared models, the FCCf structure in (c) shows the best overall agreement with both the real-space atomic arrangement and the fast Fourier transform pattern observed in Fig. 5c of the main text. As shown in Table S4, the SSE for the diffraction pattern of the FCCf structure is substantially smaller than those of the distorted HCP Re models.

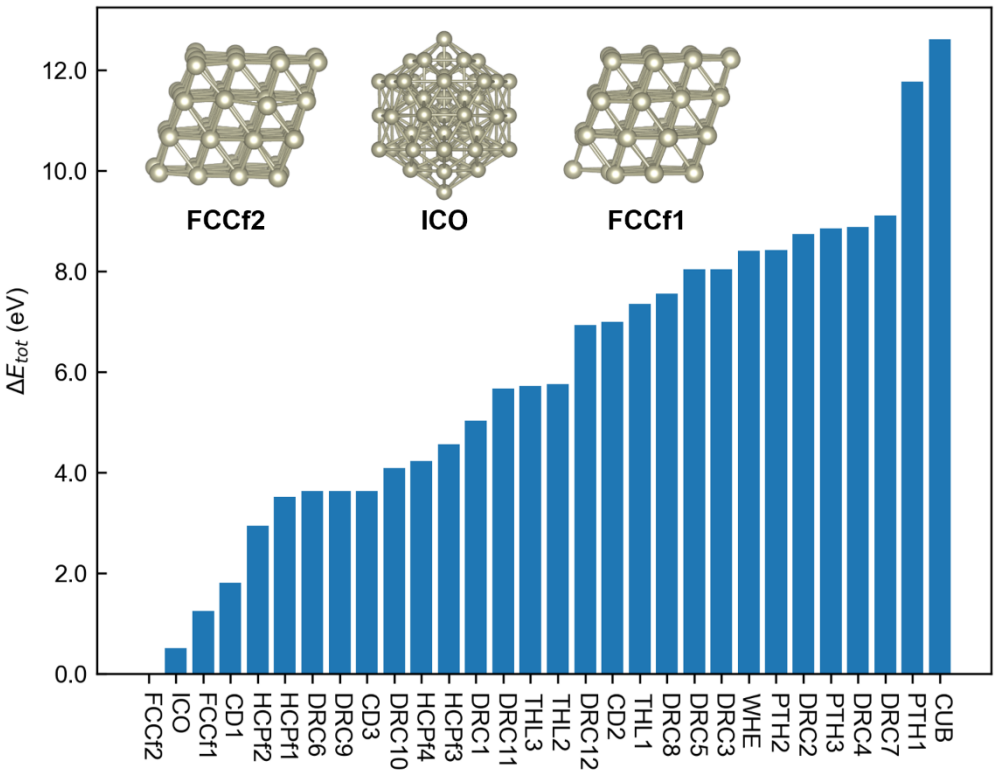

Figure S15 Relative total energies (ΔE_{tot}) of the Re_{55} clusters with respect to the face-centered cubic fragment2 (FCCf2) structure, which has the lowest energy among the 30 configurations. The names of each structure follow the notation of the 55-atom metal nanoclusters presented previously.[11] The structurally optimized geometries of the three lowest-energy structures (FCCf2, icosahedron, and face-centered cubic fragment1: FCCf1) are shown as insets.

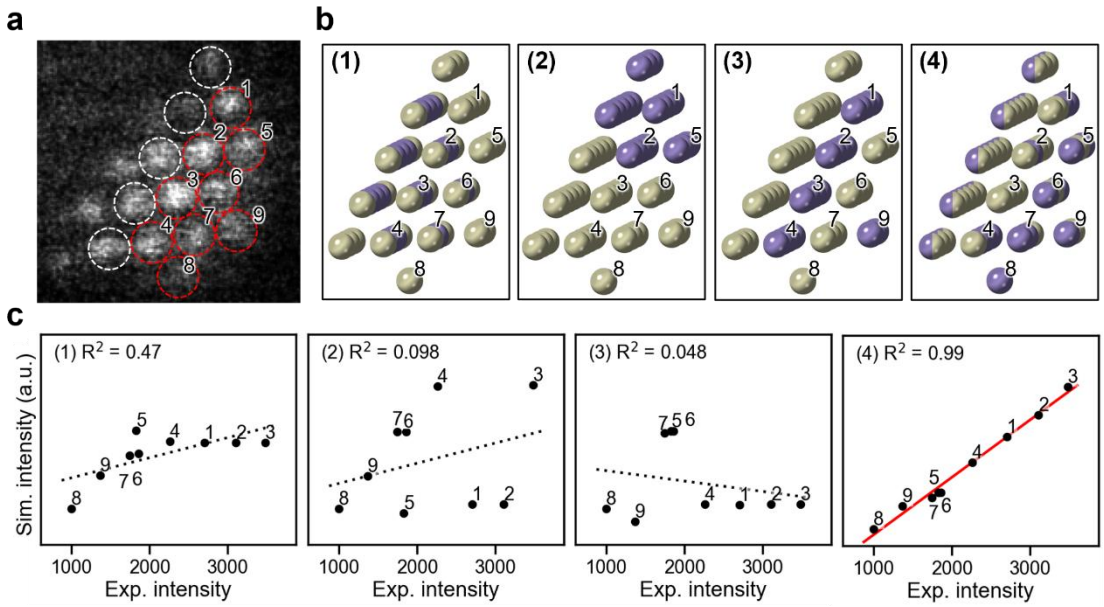

Figure S16 Analysis of the mixing pattern in a Re-Ge nanoparticle after hydrogen reduction. (a) High-angle annular dark-field scanning transmission electron microscopy image of the nanoparticle selected for analysis. A structural model based on the face-centered cubic fragment (FCCf) structure was constructed for the atomic columns enclosed by the dashed circles. The atomic columns enclosed by the red circles, which protrude from the support surface and are thus expected to have minimal signal contribution from the support, were used for quantitative image-intensity analysis. The numbers label each atomic column. (b) Atomic models of the FCCf-based nanoparticle, created according to the major atomic ordering patterns in bimetallic nanoalloys.[12,13] The models shown are: (1) Re-shell/Ge-core, (2) subcluster-segregated, (3) ordered alloy, and (4) experimentally optimized model. Atom colors: Re (beige), Ge (purple). In model (4), atoms with ambiguous elemental assignments due to overlapping with the TiO_2 support are bicolored. (c) Scatter plot comparing the experimentally measured intensities with those obtained from multi-slice simulations at the nine selected atomic columns. Numbers next to the markers denote the index of each measurement point. The experimental intensity was calculated using a two-dimensional Gaussian fit. Simulation intensities were calculated using spot intensities at atomic coordinates. A linear regression analysis was performed, and the resulting coefficient of determination (R^2) is displayed, indicating the degree to which the simulated contrast reproduces the experimental values.

Note:

The FCCf-based models were constructed as hemispheres with a diameter estimated from the experimental image. For models (1)-(3), the composition was set to be Re-rich, consistent with the overall composition determined by scanning transmission electron microscopy-energy dispersive X-ray spectroscopy (STEM-EDS). The Ge-shell/Re-core model was not considered, as it implies a Ge-rich composition inconsistent

with our EDS analysis. In model (4), the composition and atomic arrangement within each column were chosen to achieve the best possible match between the experimental and calculated intensities, aiming for an R^2 value close to 1. The resulting atomic arrangement showed no clear ordering, consistent with a random alloy in which Re and Ge atoms are mixed at the atomic level. The local atomic ratio in the assigned atomic columns 1-9 of model (4) was approximately Ge/Re = 1, differing from the Re-rich composition. This local composition is based on 28 of the 49 atoms (approximately 57 %) in the hemispheric model (4). This deviation from the average composition is considered to be a local compositional fluctuation due to the formation of a random alloy.

References

1 M. Newville, *J. Phys.: Conf. Ser.*, 2013, **430**, 012007.

2 CCDC 904024, *Russian Journal of Inorganic Chemistry*, 2013, **58**, 637–642.

3 AMCSD 11771, *Crystal Structures*, 1963, **1**, 239–444.

4 *J. Less-Common Met.*, 1982, **84**, 87–91.

5 G. S. Smith and P. B. Isaacs, *Acta Crystallographica*, 1964, **17**, 842–846, COD 9007477.

6 A. S. Cooper, *Acta Crystallographica*, 1962, **15**, 578–582, COD 9011050.

7 A. Genc, J. Marlowe, A. Jalil, D. Belzberg, L. Kovarik and P. Christopher, *Ultramicroscopy*, 2025, **271**, 114116.

8 S. B. Rice, C. Chan, S. C. Brown, P. Eschbach, L. Han, D. S. Ensor, A. B. Stefaniak, J. Bonevich, A. E. Vladár, A. R. Hight Walker, J. Zheng, C. Starnes, A. Stromberg, J. Ye and E. A. Grulke, *Metrologia*, 2013, **50**, 663–678.

9 *Materials Data on Re by Materials Project*, LBNL Materials Project; Lawrence Berkeley National Laboratory (LBNL), Berkeley, CA (United States), 2020.

10 D. C. Palmer, *J Appl Cryst*, 2020, **53**, 860–860.

11 M. J. Piotrowski, C. G. Ungureanu, P. Tereshchuk, K. E. A. Batista, A. S. Chaves, D. Guedes-Sobrinho and J. L. F. Da Silva, *J. Phys. Chem. C*, 2016, **120**, 28844–28856.

12 R. Ferrando, J. Jellinek and R. L. Johnston, *Chem. Rev.*, 2008, **108**, 845–910.

13 K. D. Gilroy, A. Ruditskiy, H.-C. Peng, D. Qin and Y. Xia, *Chem. Rev.*, 2016, **116**, 10414–10472.